

Numerical Investigation of Compressive Stress and Wettability Effects on Fluid Transport in Polymer Electrolyte Membrane Fuel Cell Porous Layers

Yanyao Bao, Zhongzheng Wang, and Yixiang Gan*

The performance of polymer electrolyte membrane fuel cells (PEMFCs) is greatly influenced by the residual water content generated during the cell operation. A comprehensive understanding of water management at the interfacial regions of PEMFC components is critical for elevating the efficiency of PEMFCs. Herein, the liquid transport and accumulation at the interfacial region of 2D microporous layer (MPL) and catalyst layer (CL) are investigated numerically, considering the effects of compression stress, porosity, and wettability. The numerical scheme is assembled by finite element method (for interfacial contact mechanics) and lattice Boltzmann method (for multiphase flow and permeability calculation). Different levels of compression stress derived from fuel cell assembly pressure are applied on the MPL/CL components, which consequently lead to variations in the pore size distribution and porosity change of the MPL/CL. The results highlight the importance of considering porosity change in the compression process, where increasing compression stress significantly decreases the liquid saturation in the MPL and interfacial gap region. Additionally, strong hydrophobicity can alleviate the heterogeneity of liquid accumulation at the MPL/CL interfacial region. The liquid and gas relative permeability are also investigated to assess the liquid drainage and fuel supply efficiency with different compression stress.

1. Introduction

The surging demand in power generation and increasing awareness for mitigating global climate change have challenged researchers to replace traditional fossil fuels with clean and renewable energy resources. New energy conversion solutions have been widely investigated, and numerous renewable energy sources have been developed, such as wind energy,^[1] water energy,^[2] and solar thermal energy.^[3] Hydrogen fuel cells have demonstrated potential for mobile and residential applications as eco-friendly energy devices.^[4] In recent years, polymer electrolyte membrane fuel cells (PEMFCs) have outstood various types of fuel cells due to several advantages, including relatively high energy efficiency, low operation temperature, and noise reduction.^[5,6] The generated water content at the cathode side greatly influences the performance of PEMFC during the operation, and a comprehensive understanding of water management is critical for elevating the

efficiency of PEMFCs.^[7] The membrane needs to be sufficiently hydrated to facilitate proton conductivities while pathways for fuel distributed into the membrane could be blocked with excessive water. Water management and liquid transport in cell components have been extensively studied to improve the performance of PEMFCs.^[8,9]

The liquid accumulation at the interfacial gaps between PEMFC components accounts for a substantial part of water flooding.^[10,11] The microporous layer and catalyst layer (MPL/CL) interface is of particular interest among the component interfaces due to the influence on cell performance and durability.^[12–15] The imperfect contact at the MPL/CL interface is often observed due to the intrinsic elasticity and surface roughness of both MPL and CL, and the resulting interfacial voids usually decrease contact area and impede ohmic and mass transport.^[16,17] The roughness nature of MPL and CL has been characterized in multiple studies with root mean square (RMS) roughness at the scale of micrometers, and the void size up to 10 µm at the MPL/CL interfacial region has been observed.^[18–20] Turhanet et al.^[21] analyzed water distribution and transport at PEMFC components and interfaces considering component surface morphology and cracks. Liquid storage was observed at the

Y. Bao, Y. Gan
School of Civil Engineering
The University of Sydney
Camperdown, NSW 2006, Australia
E-mail: yixiang.gan@sydney.edu.au

Z. Wang
School of Mechanical, Medical and Process Engineering
Faculty of Engineering
Queensland University of Technology
Brisbane, QLD 4001, Australia

Y. Gan
The University of Sydney Nano Institute (Sydney Nano)
The University of Sydney
Camperdown, NSW 2006, Australia

 The ORCID identification number(s) for the author(s) of this article can be found under <https://doi.org/10.1002/ente.202201028>.

© 2022 The Authors. Energy Technology published by Wiley-VCH GmbH. This is an open access article under the terms of the Creative Commons Attribution-NonCommercial License, which permits use, distribution and reproduction in any medium, provided the original work is properly cited and is not used for commercial purposes.

DOI: [10.1002/ente.202201028](https://doi.org/10.1002/ente.202201028)

MPL/CL interface, suggesting a significant influence of surface roughness and cracks on water accumulation and transport. Kalidindi et al.^[20] studied the influence of MPL/CL interfacial gaps on the performance of PEMFC numerically with interface profiles acquired from experimental measurements. Liquid accumulation and mass transport resistance were identified due to contact area loss with interfacial voids. Swamy et al.^[16] investigated the effects of the MPL/CL interfacial gaps on the ohmic and mass transport reduction of PEMFC. An analytical model adapting experimentally measured interface profile data was developed, where a substantial amount of water was observed at the MPL/CL interface. Their model also predicts that contact resistance and water accumulation can be alleviated with a 50% reduction in surface roughness at the interface. In addition, Weber et al.^[22] and Hartnig et al.^[23] also observed water accumulation at the MPL/CL interfaces using neutron imaging and X-ray radiography, and the concerns regarding cell durability were raised as a result of the flooding at component layer interfaces.

Moreover, due to the inherent rough nature of PEMFC component interfaces, the assembly pressure of the fuel cell stack should be carefully controlled because the compressive stress can significantly affect the performance of PEMFCs.^[24–26] While the assembly pressure needs to be sufficiently large to avoid sealing problems such as fuel leakage, internal combustion, and undesired contact resistance, the overloaded pressure could increase gas diffusion resistance and even leads to structure damage of membrane and diffusion layers.^[24] The assembly pressure of cell stacks usually varies from 0.18 to 2 MPa, and the compression ratio can range between 10% and 50% depending on the assembling specifications.^[25,26] The PEMFC performance has been compared with different compression conditions, and some researchers suggest that the compression ratio of 14% best facilitates the PEMFC performance in terms of current density.^[24,26] Particularly, the mass transport of gas and liquid phase is influenced by different compression stress due to the change of material porosity and pore size distribution.^[25,27–31] Bazylak et al.^[29] investigated water flow inside the gas diffusion layer (GDL) under various compression conditions. The results suggest that compressing GDL leads to fiber breakup and decrease of material hydrophobicity. Fazeli et al.^[30] studied the influence of compression on liquid and reactants transport of PEMFC numerically with discussions on the optimized compression values for water and oxygen distribution. Atkinson et al.^[25] examined the current density and cell voltage of PEMFC under different compression stress. The results indicate that the initial void volume and thickness of MPL play a vital role in the oxygen diffusivity inside diffusion media.

However, very few studies have focused on the liquid and gas transport and at the MPL/CL interfacial gap under different compression stress. This mainly attributes to the complexities of modeling the morphology of porous surfaces as well as coupling the contact mechanics of the porous layers and fluid transport within the pore space and interfacial region. To tackle these, we propose a subsequently coupled finite element method (FEM)-lattice Boltzmann method (LBM) approach to explicitly model the effects from contact mechanics of layer interfaces. In this article, the liquid transport and accumulation at the MPL/CL interface of PEMFC are investigated numerically. First, the MPL/CL interface profile is generated computationally

with surface roughness and pore size distribution comparable to realistic MPL and CL material properties. Second, the surface contact and subsequent deformation under different compressive stress are simulated with the FEM. Then, the resulting MPL/CL interfacial morphology is implemented in the multiphase flow model using the LBM to examine the effect of compression on liquid transport and accumulation. The porosity change of pore space under various loading conditions is also incorporated, and the corresponding influences on liquid transport are investigated. Based on LBM simulations of single- and multiphase flows, the relative permeability of water and gas is calculated throughout the liquid draining process to assess the liquid discharge and fuel feeding efficiency. In addition, the effect of material wettability is investigated to compare the liquid and gas flow conditions with varied component hydrophobicity.

2. Methodology

In this work, we employ FEM and LBM to investigate the deformation of rough interfaces and its impact on the subsequent multiphase flow transport, respectively, between porous layers under different compression stresses. To further simplify the computational models, several assumptions are made to generalize the problem and extend the range of physical parameters and control variables, such as porosity, wettability, and compressive loading levels. The MPL and CL are assumed to be isotropic material with homogeneous wettability and porosity. The CL is treated to have the same material properties as MPL, such as elasticity and porosity for the convenience of contact and multiphase flow modeling, due to the similarity of their intrinsic properties. The mechanical contact between MPL and CL is assumed to be elastic contact, and the adhesion effects of contacting surfaces due to hot-pressing process are neglected. The elasticity of MPL is assumed as purely elastic, although some plastic deformation may occur to MPL.^[32] The simulations are conducted in 2D and isothermal conditions, aiming to achieve qualitative trends with respect to the control variables.

2.1. Surface Roughness and Contact Mechanics

The roughness nature of MPL and CL has been reported in several studies with root mean square roughness (R_q) and average arithmetic roughness (R_a) usually in the range of several micrometers.^[16,18,19] In this study, the rough surfaces are reconstructed with Gaussian height distribution function and autocovariance function, and R_q of the generated MPL and CL surface is calculated as 5.86 and 3.17 μm , respectively, which is comparable to experimental reported values.^[18] The details of rough surface generation can be found in ref. [33]. The generated surfaces are imported in the surface contact model, where the MPL/CL interfacial morphology under various compression conditions is simulated using the FEM software ABAQUS/Explicit.

In the FEM model, Young's modulus (E_y) and Poisson's ratio of the applied MPL and CL material are determined as 30 MPa and 0.35, which are comparable to the reported values in ref. [34]. The thickness of MPL and CL is 18 and 15 μm , respectively, and the model length is 1000 μm , which is sufficient to capture the representative contact behavior. MPL is placed above the CL with

an initial separation of $1\text{ }\mu\text{m}$, and then a downward displacement load is prescribed on the top boundary of MPL with velocity of $1\text{ }\mu\text{m s}^{-1}$. Dynamic explicit time step is applied for the contact model. Part of the interfacial region under compression with stress contour is shown in **Figure 1**. The data used for multiphase flow are in the middle section of the contact model to avoid boundary effects from two sides, where the length of each section is $100\text{ }\mu\text{m}$. Three simulation cases of FEM surface contact are conducted to obtain sufficient data for result analysis, which makes the total length of surface morphology used for multiphase flow simulation $300\text{ }\mu\text{m}$. Though the R_q of three surface profiles is statistically similar, the realization of local surface asperities is different for each case.

In the surface contact model, interfacial morphologies at four different compression levels are selected for pore structure generation and multiphase flow modeling at the MPL/CL interface. Applying different levels of compression loading can reflect the cell assembly pressure as well as the location of porous layers (under ribs or flow channel). Normalized compression stress (NS) is introduced to compare the compression levels used in this study with experimental values, considering the difference of material properties between model parameters and experimental reported values. Normalized compression stress is defined as the ratio between compression stress and Young's modulus of the MPL material. Four different stress from FEM compression simulation results are selected as [0.15, 0.27, 0.45, and 0.6 MPa], leading the corresponding NS equal to [0.005, 0.009, 0.015, 0.02]. The NS for TGP-H-060 and SGL 10BE-type GDL were calculated as 0.012 and 0.02 in refs. [29,35] when applied stress is 0.18 and 0.3 MPa, respectively. The magnitude of NS is comparable to the literature reported values, and the applied compression stress is in the range of the cell stack clamping pressure that is commonly used for the compression analysis of porous transport media in PEMFCs.^[36,37] Therefore, the corresponding surface coordinates at four compression levels with NS of [0.005, 0.009, 0.015, 0.02] are extracted for pore space generation and liquid transport modeling. It should be noted that the interfacial morphology change is minimal after reaching the normalized compression stress of 0.02 due to the increased contact resistance between the MPL and CL.

2.2. Pore Structure

The porous space of MPL and CL is generated by filling circular obstacles in the simulation domain. The porous structure

representing MPL and CL should have porosity and pore size distribution matching actual MPL and CL materials. The porosity φ is defined as the ratio of void area to total area, and controlled by the size and total number of generated circular obstacles. According to experimental measurements, the porosity of MPL ranges between 0.3 and 0.8 depending on the coating and compression conditions, and typical pore size is in the order of $10\text{--}200\text{ nm}$.^[38,39] In terms of CL, the porosity is reported from 0.5 to 0.7, and pore size is around 100 nm .^[40\text{--}42] Two different scenarios for component porosity are considered in this work. For the first scenario, the porosity of MPL and CL is fixed as 0.72 regardless of the change of compression stress. For the second scenario, the porosity decreases with the increase of compression stress. In principle, the porosity of porous layers decreases with the increase of compression loading. By considering the constant porosity model here, we can evaluate the influence of geometry variations on the fluid transport behaviors under various compression conditions. The selected porosities should reflect the variation of pore sizes at different compression conditions, while the small pore throat size resulted from low porosity could affect the convergence of multiphase flow model algorithm. Therefore, $\varphi = [0.88, 0.8, 0.72, 0.64]$ are chosen to reflect the porosity change under various compression loading accordingly, i.e., $NS = [0.005, 0.009, 0.015, 0.02]$. Although the highest reported porosity for MPL material is 0.8 in the literature^[38] porosity of 0.88 is adopted in this work as an extreme value for modeling porous layer material and, in particular, investigating the effects of porosity change on fluid transport behaviors. The selected porosities should reflect the variation of pore sizes at different compression conditions, allowing the range of pore size changes while maintaining the convergence of multiphase flow model algorithm. Note that the model regarding the porosity change is simplified; further study combining accurate poromechanics formulations can be adopted.

It is assumed that MPL and CL have identical porosity and pore size distribution under the same compression condition. Then the obstacles are generated randomly in the simulation domain with the diameter of 154 nm , and a minimum distance of 10 nm is prescribed between each obstacle to avoid overlap. The diameter and minimum distance between obstacles are chosen to generate the porous structures with appropriate pore size distribution and porosity to match the MPL material that typically used in PEMFC, e.g., acetylene black.^[43,44] The selected values also assist to avoid extreme small pore throat size which could influence the stability of fluid flow simulation with LBM

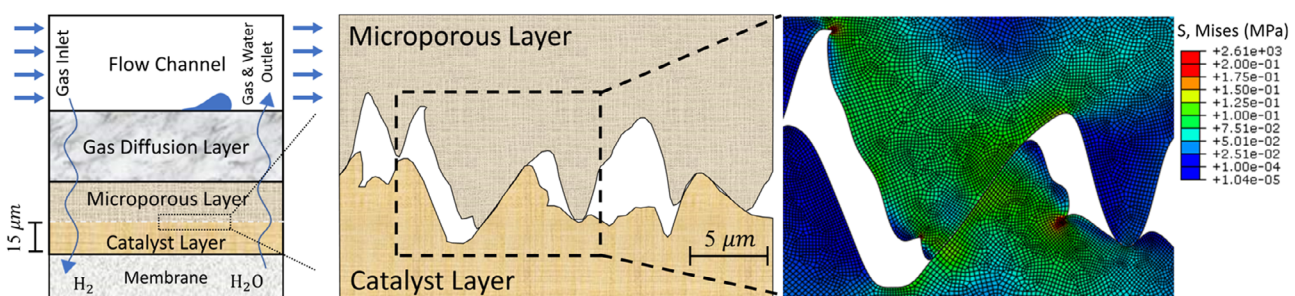


Figure 1. A multiscale schematic for PEMFC component layers. The rough surfaces of MPL and CL are reconstructed and implemented into the FEM model for surface contact simulation, where interfacial region under compression with stress contour is presented.

algorithm. The pore size is defined as the radius of circle inscribed in the pore space, and an automated watershed algorithm is applied to calculate the pore size distribution of generated porous domain.^[45] Figure 2a shows the pore size distribution and average pore size of generated pore spaces with four different porosities. The results suggest that the average pore size of the generated porous medium from 109 to 255 nm is comparable to experimentally measured values in the literature, which was reported in the range of 200 nm for MPL-only material.^[38] In addition, the pore size in this work is also consistent with values adopted in numerical study.^[39] In the following, the MPL and CL surface profiles derived from the FEM contact model are implemented to the porous medium. The interfacial gap is introduced by removing the circular obstacles whose centers are bounded by the MPL and CL surfaces, and a typical reproduced MPL/CL interfacial region is demonstrated in Figure 2b.

2.3. Fluid Transport

The liquid transport at the MPL/CL interfacial region is simulated using the LBM with D2Q9 lattice.^[46] Based on the Bhatnagar–Gross–Krook (BGK) collision operator, each fluid component is described by the distribution function that satisfies the following equation^[47]

$$f_i^n(x + e_i \Delta t, t + \Delta t) - f_i^n(x, t) = -\frac{\Delta t}{\tau^n} (f_i(x, t) - f_i^{\text{eq}}(x, t)) \quad (1)$$

where f_i^n is the density distribution function for n^{th} fluid component in the i^{th} direction, and τ^n is the single relaxation frequency of n^{th} component. The kinematic viscosity is given as $\nu^n = (\tau^n - 0.5)c_s^2 \Delta t$, where c_s is the speed of sound. The equilibrium distribution f_i^{eq} of n^{th} fluid component is calculated by

$$f_i^{\text{eq}}(x, t) = \omega_i \rho_n \left[1 + \frac{e_i \Delta u^{\text{eq}}}{c_s} + \frac{(e_i \Delta u^{\text{eq}})^2}{2c_s^4} - \frac{(u^{\text{eq}})^2}{2c_s^2} \right] \quad (2)$$

where ω_i is the weight for the i^{th} direction with $\omega_i = \frac{4}{9}$ ($i = 1$), $\omega_i = \frac{1}{9}$ ($i = 2, 3, 4, 5$), and $\omega_i = \frac{1}{36}$ ($i = 6, 7, 8, 9$).

u^{eq} represents the macroscopic equilibrium fluid velocity, and ρ_n is the density of the n^{th} component. For the D2Q9 model, the discrete velocities e_i are given by

$$[e_1, e_2, e_3, e_4, e_5, e_6, e_7, e_8, e_9] = c_u \begin{bmatrix} 0 & 10 & -1 & 0 & 1 & -1 & 1 \\ 0 & 0 & 1 & 0 & -1 & 11 & -1 & -1 \end{bmatrix} \quad (3)$$

where c_u denotes the ratio of lattice spacing Δx and time step Δt . The local density ρ_n and equilibrium velocity u^{eq} can be written as

$$\rho_n = \sum_i f_i^n \quad (4)$$

$$u^{\text{eq}} = u' + \frac{\tau^n F_n}{\rho_n} \quad (5)$$

where $u' = \frac{\sum_n \left(\sum_i \frac{f_i^n e_i}{\tau^n} \right)}{\sum_n \frac{\rho_n}{\tau^n}}$, and F_n is the total force acting on the n^{th} component including interaction force $F_{\text{inter},n}$ introduced by surface tension and adhesion force $F_{\text{ads},n}$ introduced by wettability.

The Shan–Chen multicomponent model introduces an interaction force as

$$F^{\text{sc}(n)}(x) = -\psi^n(x) \sum_{\tilde{n} \neq n} G_{\tilde{n}n} \sum_i \omega_i \psi^{\tilde{n}}(x + e_i \Delta t) e_i \Delta t \quad (6)$$

where ψ^n is the effective density function for the n^{th} component, and scalar G controls the strength of the particle–particle interaction. The value of G should be positive to generate repulsive force between different components. The contact angle in the model can be modified by adjusting the artificial density of walls.^[48]

The dimension of the simulation domain is $M \times N = 10000 \times 1200$ lu² (lu denotes lattice unit), and the diameter of circular obstacles is 15.4 lu. A section of the simulation domain for LBM modeling is shown in Figure 3a. CL size is fixed by positioning the lowest surface curvature coordinate

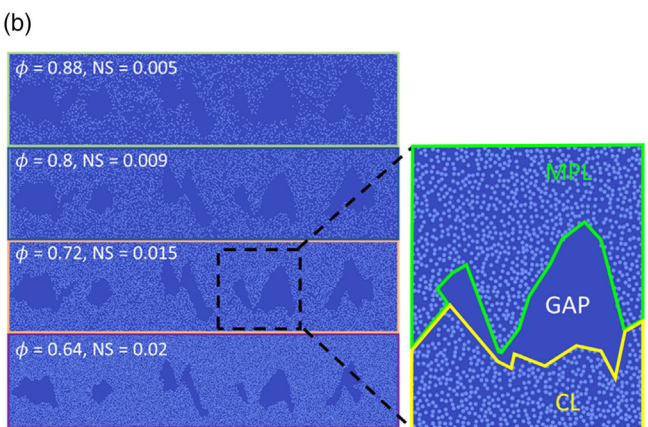
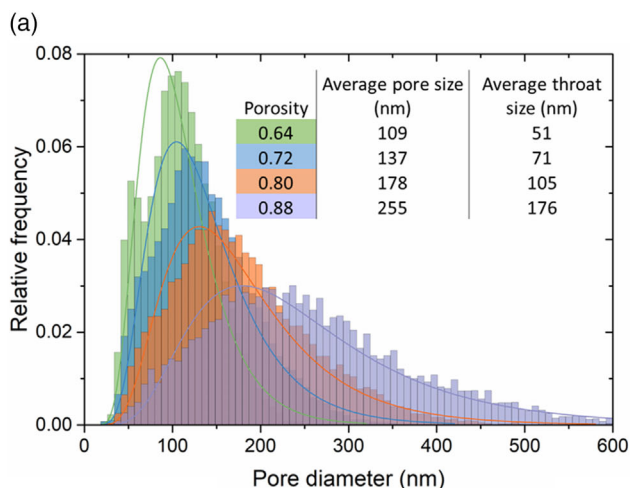


Figure 2. a) Pore size distribution of the generated MPL/CL porous structure with $\varphi = [0.88, 0.8, 0.72, 0.64]$; b) MPL/CL interfacial region with different porosities under various compression loading.

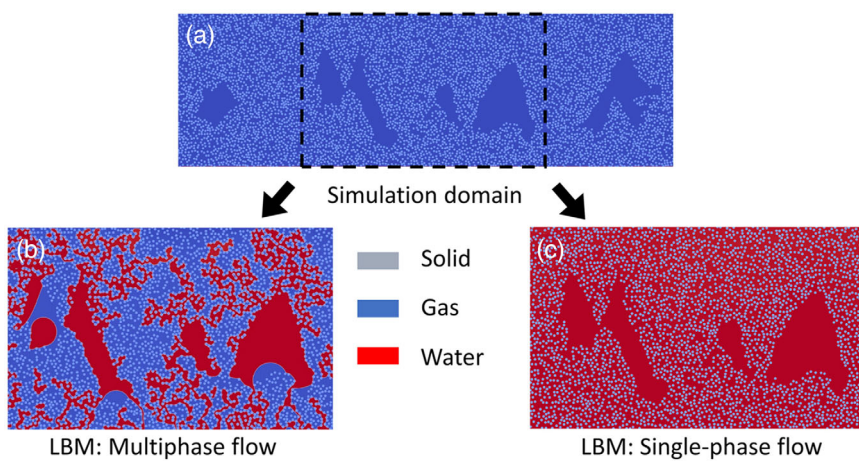


Figure 3. a) Simulation domain for liquid transport at a typical MPL/CL interfacial region; b) a snapshot of liquid transport and accumulation at the interfacial region; c) LBM simulation of single-phase flow for intrinsic permeability calculation.

200 lu measuring from the bottom boundary, and the thickness of MPL decreases with the increase of compression stress as the space of interfacial gap is occupied by MPL. The fluid–fluid interfacial tension in Shan–Chen model is determined by interparticle strength G_{in} ,^[49] and the resultant interfacial tension γ between water and gas is 0.137 lu calculated with Young–Laplace equation. The contact angle θ of circular obstacles is set to 140° or 100° by adjusting the wall density. The benchmark test of interfacial tension and contact angle is shown in Figure 4. The kinematic viscosity ν of both phases is 0.167 lu by setting the relaxation time equal to 1.^[50] According to the existing literature,^[51–53] the pore-scale capillary number ($Ca = \frac{\nu_{in}\eta}{\gamma}$, where η is the dynamic viscosity) and Reynolds number ($Re = \frac{\rho_1 v_{in} d_o}{\gamma}$, where ρ_1 is the liquid density and d_o is obstacle diameter) for multiphase flow in PEMFCs are in the order of 10^{-5} and 10^{-4} , respectively, indicating an interfacial tension dominated flow regime over the viscous and inertia force. We aim to reproduce the fluid properties and conditions to ensure the modeled multiphase flow in the interfacial tension dominated flow regime, i.e., $Ca \approx 10^{-5}$ and $Re \approx 10^{-4}$. This would allow us to investigate the effects of compression stress and wettability on fluid

transport at the MPL/CL interfacial region in a setup that is comparable to the actual flow condition of an operating PEMFC. As a result, the inlet velocity for liquid water is consequently chosen as $v_{in} = 0.0005$ lu, resulting in $Ca = 6.09 \times 10^{-4}$ and $Re = 0.056$, respectively. The employed capillary number and Reynolds number are higher than actual values in an operating PEMFC, but the values in current model are small enough to ensure capillary-dominant flow condition and to ignore the inertial and viscous effects. As the inertial and viscous effects are negligible for the simulated multiphase flow, the density ratio and dynamic viscosity ratio between gas and liquid water are set to 1 in the simulation as the liquid flow is dominated by the interfacial tension. Therefore, the gas phase in this work can be perceived as either air (at the cathode side) or hydrogen (at the anode side) to provide insights on the gas transport under various compression conditions of PEMFC. Periodic boundary condition is prescribed on both sides of the simulation domain, and pressure outlet boundary condition is employed at the top boundary.

The lattice unit is converted to physical values by applying three reference quantities, i.e., length scale $l_0 = 10^{-8}$ m, time scale $t_0 = 10^{-6}$ s, and mass scale $m_0 = 10^{-13}$ kg. Consequently,

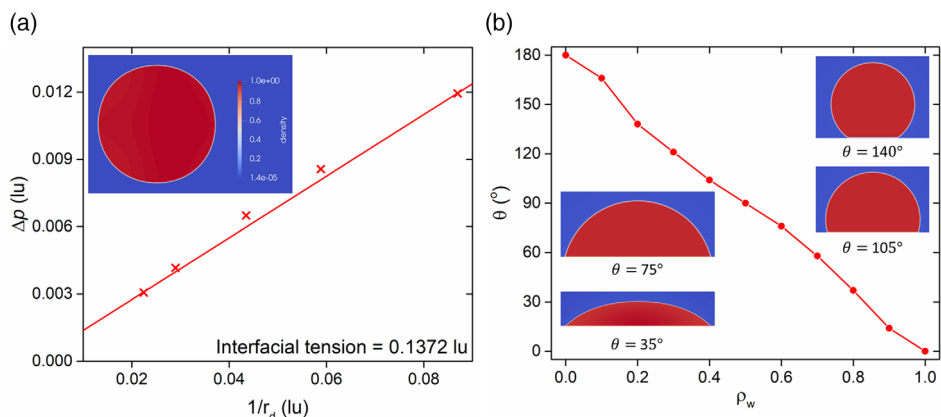


Figure 4. a) Pressure drop Δp across the interface of 2D liquid droplets for different radius r_d ; b) contact angle of droplet formed on solid surfaces with different wall density ρ_w .

the dimension of simulation domain size becomes $100 \times 12 \mu\text{m}^2$ with obstacle diameter of 154 nm, and the inlet velocity of liquid water is $5 \mu\text{m s}^{-1}$. Water–gas interfacial tension is 13.7 mN m^{-1} , and the dynamic viscosity of fluid is 1.67 Pa s . Note that the selection of these quantities aims to have a situation of $\text{Ca} = 6.09 \times 10^{-4}$ and $\text{Re} = 0.056$. Geometrical parameters of the modeled MPL/CL interfacial region and fluid properties are summarized in **Table 1**. Therefore, the pore structure generated in the previous section can be directly implemented to the LBM model with the same geometrical parameters. All simulation cases stop at $t = 45 \text{ s}$ with output interval of 1 s. The simulation length ensures the presentation of liquid transport phenomenon covering both start-up and stable operation stage of PEMFC, considering the limitation of computational resources allocated. Open-source package OpenLB is used to simulate the liquid transport at the MPL/CL interfacial region.^[54] **Table 2** summarizes parameter setup for all LBM simulation cases.

2.4. Relative Permeability Calculation

The relative permeability of liquid water and gas at different saturation level can be calculated based on LBM simulations of multi- and single-phase flow results.^[50] First, the volume-averaged fluxes of liquid water q_w and gas q_g are derived by

$$q_w = \frac{1}{M \cdot N} \sum_{i=0}^{n_w} U_{ywi}, \quad q_g = \frac{1}{M \cdot N} \sum_{i=0}^{n_g} U_{ygi} \quad (7)$$

where n_w and n_g are total lattice number of liquid and gas; U_{ywi} and U_{ygi} are velocity of i th liquid and gas lattice node in the y -direction, respectively. The lattice nodes of liquid and gas phase are identified by local density, and the interfacial nodes are excluded from the flux calculation due to spurious velocity. The relatively permeability of liquid water (k_{rw}) and gas (k_{rg}) is calculated as follows^[55]

$$k_{rw} = \frac{q_w \nu_w}{k_{satg}}, \quad k_{rg} = \frac{q_g \nu_g}{k_{satg}} \quad (8)$$

where ν_w and ν_g are the kinematic viscosity of liquid and gas phase, and g is the gravitational force. $k_{sat} = \frac{q_{sat} \nu_{sat}}{g}$ is the intrinsic permeability which can be measured by single-phase flow simulation of the porous domain, with q_{sat} and ν_{sat} being the volume-

Table 1. Geometrical parameters of modeled MPL/CL interfacial region and fluid properties.

Parameters	Lattice unit	Physical unit	
Domain size	10000×1200	l_0^2	$100 \times 12 \mu\text{m}^2$
Obstacle diameter	15.4	l_0	154 nm
Fluid density	1	$\text{m}_0 l_0^{-2}$	1000 kg m^{-3}
Fluid dynamic viscosity	0.167	$\text{m}_0 l_0^{-1} t_0^{-1}$	1.67 Pa s
Water/gas interfacial tension	0.137	$\text{m}_0 t_0^{-2}$	13.7 mN m^{-1}
Water injection velocity	0.0005	$l_0 t_0^{-1}$	$5 \mu\text{m s}^{-1}$
Capillary number	6.09×10^{-4}	—	6.09×10^{-4}
Reynolds number	0.056	—	0.056

Table 2. Parameter setup for all simulation cases. $\varphi = f(\text{NS})$ represents the porosity change under different compression stress applied, where $\varphi = [0.88, 0.8, 0.72, 0.64]$ corresponds to $\text{NS} = [0.005, 0.009, 0.015, 0.02]$.

Group	Normalized stress (NS)	Porosity (φ)	Contact angle (θ)	Sample length (M) [μm]	Number of cases simulated
$\theta = 140^\circ$, $\varphi = 0.72$	0.005	0.72	140°	100	3
	0.009	0.72	140°	100	3
	0.015	0.72	140°	100	3
	0.02	0.72	140°	100	3
$\theta = 140^\circ$, $\varphi = f(\text{NS})$	0.005	0.88	140°	100	3
	0.009	0.8	140°	100	3
	0.015	0.72	140°	100	3
	0.02	0.64	140°	100	3
$\theta = 100^\circ$, $\varphi = 0.72$	0.005	0.72	100°	100	1 ^{a)}
	0.009	0.72	100°	100	1
	0.015	0.72	100°	100	1
	0.02	0.72	100°	100	1
$\theta = 100^\circ$, $\varphi = f(\text{NS})$	0.005	0.88	100°	100	1
	0.009	0.8	100°	100	1
	0.015	0.72	100°	100	1
	0.02	0.64	100°	100	1

^{a)}In groups with $\theta = 140^\circ$, three cases are conducted for each setup. For groups with $\theta = 100^\circ$, one case is conducted by changing the contact angle of its counterpart in group with $\theta = 140^\circ$ to 100° while keeping all other parameters same.

averaging flux and kinematic viscosity. The lattice Boltzmann simulations of single-phase flow are conducted on the corresponding MPL/CL interfacial region with four different compressive stress. The intrinsic permeability is calculated at time step of 5.0×10^4 with the single-phase flow flux residual smaller than 10^{-4} lu. A section of steady-state single-phase flow saturation profile is shown in Figure 3c.

3. Results and Discussion

This section presents four different aspects focusing on the liquid and gas transport behaviors: 1) pore-scale liquid displacement mechanisms; 2) effects of compression stress on liquid transport; 3) effects of wettability on liquid accumulation; and 4) relative permeability assessments under various operational conditions. The liquid invasion process through the MPL/CL interfacial region is described, and pore-scale displacement mechanisms such as droplet merge and snap-off are observed due to the capillary pressure difference in pores and throats. The temporal evolution of liquid saturation at MPL/CL interface under various compression stress is examined considering two different scenarios: 1) a fixed porosity model with only geometrical variations in the interfacial voids, and 2) a stress-dependent porosity model corresponding to various loading conditions applied. In addition, the effects of wettability on liquid accumulation are investigated by changing the contact angle of solid obstacles from 140° to 100° , and liquid saturation at interface

layers is presented and compared. Finally, the liquid and gas relative permeability under different porosity and wettability throughout the liquid drainage process is evaluated, and a relative permeability equation is applied to assess the liquid discharge and fuel supply efficiency.

3.1. Liquid Transport Characteristics

Figure 5 presents the liquid water distribution inside a typical MPL/CL interfacial region at different timesteps, with MPL, CL, and the interfacial gap as bounded area by MPL and CL surface denoted in the corresponding area. Water is injected with a low speed of $5\mu\text{m s}^{-1}$ into the CL from the bottom boundary, and capillary fingering is observed in Figure 5a due to the relatively small Ca of liquid flow ($\text{Ca} = 6.07 \times 10^{-4}$). Part of the water clusters in the CL reaches the interfacial gap between MPL and CL, and liquid droplets are formed at the upper boundary of CL with the accumulation of water. The droplets in the interfacial gap keep expanding and merge with other droplets during the pore-filling process. In the meanwhile, snap-off is observed as liquid invading the pore space, where some droplets are disconnected from the water clusters in the CL and move up in the interfacial gap, as shown in Figure 5b,c. Snap-off is a pore-scale displacement mechanism caused by the pressure nonequilibrium at the pore throat channel, resulting in the breakup of the continuous flow when a nonwetting fluid displaces a wetting

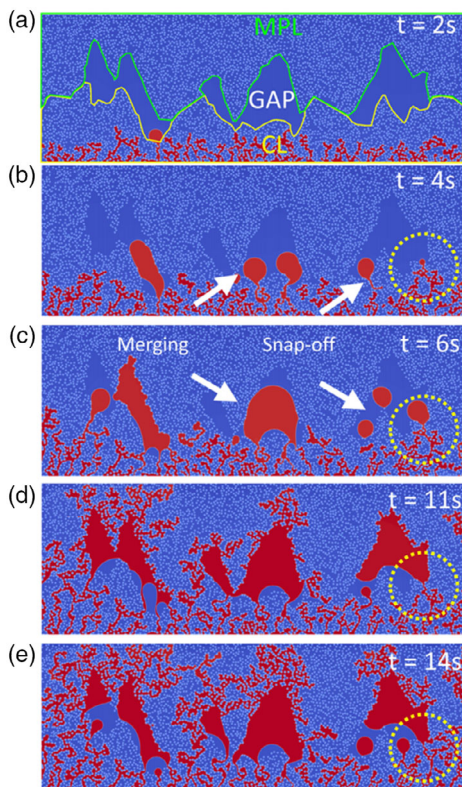


Figure 5. Evolution of water clusters at a typical MPL/CL interfacial region, showing merging (a–c), snap-off (b–c), and cluster growth (b–e) throughout the liquid displacement process. The parameters for the presented simulation are $\text{NS} = 0.015$, $\varphi = 0.72$, and $\theta = 140^\circ$.

fluid.^[56,57] After the droplets snap-off, the liquid accumulates in the catalyst layer and forms another droplet in the interfacial gap, as shown in Figure 5d. It is also observed that liquid flow in the porous space of CL stops developing once the water clusters reach the interfacial gap, as shown in Figure 5b–d. For instance, the water cluster in the yellow circle developed three flow branches at $t = 4$ s. The left liquid branch first entered the interfacial gap and formed a droplet. At the same time, the other two liquid branches stopped developing and remained unchanged until the liquid inside the interfacial gap broke through into MPL pores at $t = 11$ s. Once the interfacial gap is filled with liquid, multiple water clusters are formed in the MPL, leading to a slight decrease of liquid volume in the interfacial gap. Afterward, the water clusters continue developing in the pore space of MPL and finally reach the outlet at the top of simulation domain, as shown in Figure 5e.

The abovementioned flow behaviors during the liquid displacement process are resulted from the capillary pressure difference in pores and throats. According to the Young–Laplace equation

$$P_c = P_{\text{gas}} - P_{\text{liquid}} = -\frac{2\gamma\cos\theta}{r} \quad (9)$$

where P_c is the capillary pressure, γ is the interfacial tension, r is the pore radius, and θ is the contact angle of solid obstacles. Liquid displacement occurs when P_c is larger than the local capillary pressure providing resistance to liquid invasion. The interfacial gap area and pore size of MPL/CL material reduce with the increase of compression stress, resulting in the increase of local capillary pressure in the pore space. Based on Equation (9), larger pores have smaller capillary pressure resisting the liquid invasion. Therefore, due to the relatively large pore size difference, a state of pressure nonequilibrium is observed across the CL pore space and interfacial gap, resulting in the snap-off of droplets. In addition, the capillary pressure difference is also influencing the pore-filling sequence, where the liquid flow tends to fill larger pores instead of smaller ones in the liquid displacing process. Generally, the liquid transport at the MPL/CL interfacial region follows the sequence of CL–GAP–MPL. Water clusters flowing from CL directly to MPL are hardly observed due to the relatively high capillary pressure in the MPL pore space compared to the interfacial gap.

3.2. Effects of Compression Stress

First, the temporal evolution of liquid saturation at the MPL/CL interfacial region with $\theta = 140^\circ$ and $\varphi = 0.72$ is presented in Figure 6. For the catalyst layer, the liquid saturation reaches maximum value at $t = 13$ s for all cases, and the saturation remains stable afterward. It is observed that liquid saturation increases with the increase of compression stress, which can be explained by the contact area change between CL and MPL due to different loading conditions. Higher compression stress reduces the interfacial gap area, so the water clusters are faced with higher capillary pressure between CL and MPL for liquid transport. Therefore, liquid saturation in CL is higher for the cases with higher compression stress, as more liquid is confined in the CL and flows through the small pores instead of large pores

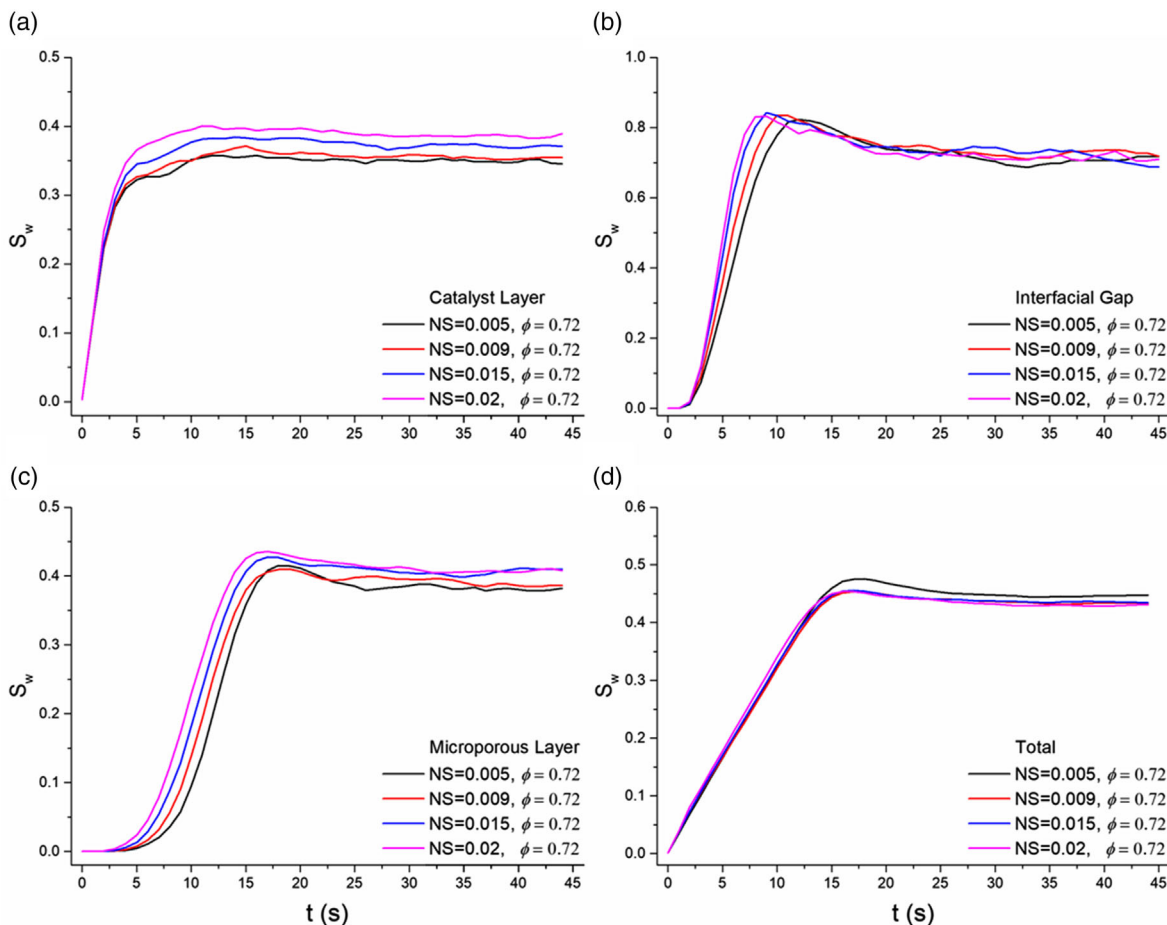


Figure 6. Temporal evolution of liquid saturation (S_w) with simulation group $\theta = 140^\circ$ and $\varphi = [0.72]$ for a) catalyst layer; b) interfacial gap; c) microporous layer; and d) total simulation domain.

of interfacial gaps. For the interfacial gap, the liquid saturation reaches the peak at around $t = 9$ s. Before reaching the maximum saturation, the higher compression stress cases have higher liquid saturation due to the reduced interfacial gap area. After reaching maximum saturation, the liquid saturation decreases as liquid develops clusters in the MPL porous space. Saturation fluctuation in the interfacial gap is observed, and no clear trend is identified for the compression stress effects on the liquid saturation in the interfacial gap for the rest of pore-filling process. For the microporous layer, the liquid saturation decreases after reaching the maximum value at $t = 17$ s as liquid flows out of the MPL domain, followed by a slight fluctuation for the rest of the liquid invading process. The liquid saturation in MPL is mainly influenced by the interfacial gap area, where high compression stress leads to a reduced interfacial gap and a higher saturation in the MPL is observed. The liquid saturation of the total MPL/CL interfacial region demonstrates all four cases have similar liquid saturation regardless of the compression stress, with a slightly higher liquid saturation observed for the case with $NS = 0.005$ due to the largest interfacial gap area in the entire domain.

Temporal evolution of liquid saturation for simulation group $\theta = 140^\circ$ and $\varphi = f(NS)$ at the MPL/CL interfacial region is

presented in **Figure 7**, where the porosity change of pore space under different loading conditions is incorporated. For the catalyst layer, the evolution of liquid saturation is quite similar to the cases with $\varphi = [0.72]$, where the liquid saturation increases with compression stress. For the interfacial gap, the maximum saturation increases with the decrease of compression stress as larger pore spaces have a higher potential for liquid accumulation. The liquid saturation decreases rapidly after reaching the maximum value, and fluctuation is observed in all cases. For the microporous layer, the liquid saturation for the case with $NS = [0.005]$ is outstandingly higher than the other three cases, suggesting the effects of porosity on liquid transport and accumulation. Porosity of the MPL component is inversely proportional to the compression stress applied. Therefore, the capillary pressure in the pore space decreases when faced with smaller compression stress, providing a favorable condition for water flowing and accumulating at the MPL domain. In terms of total saturation, increasing the compressive stress significantly decreases the liquid accumulation. The case with $NS = [0.005]$ has the highest saturation owing to the largest interfacial gap area which has liquid saturation up to 80% in the gap region, and the liquid saturation for cases with $NS = [0.009, 0.015, 0.02]$ decreases slightly with the increase of compressive stress. This trend can be qualitatively

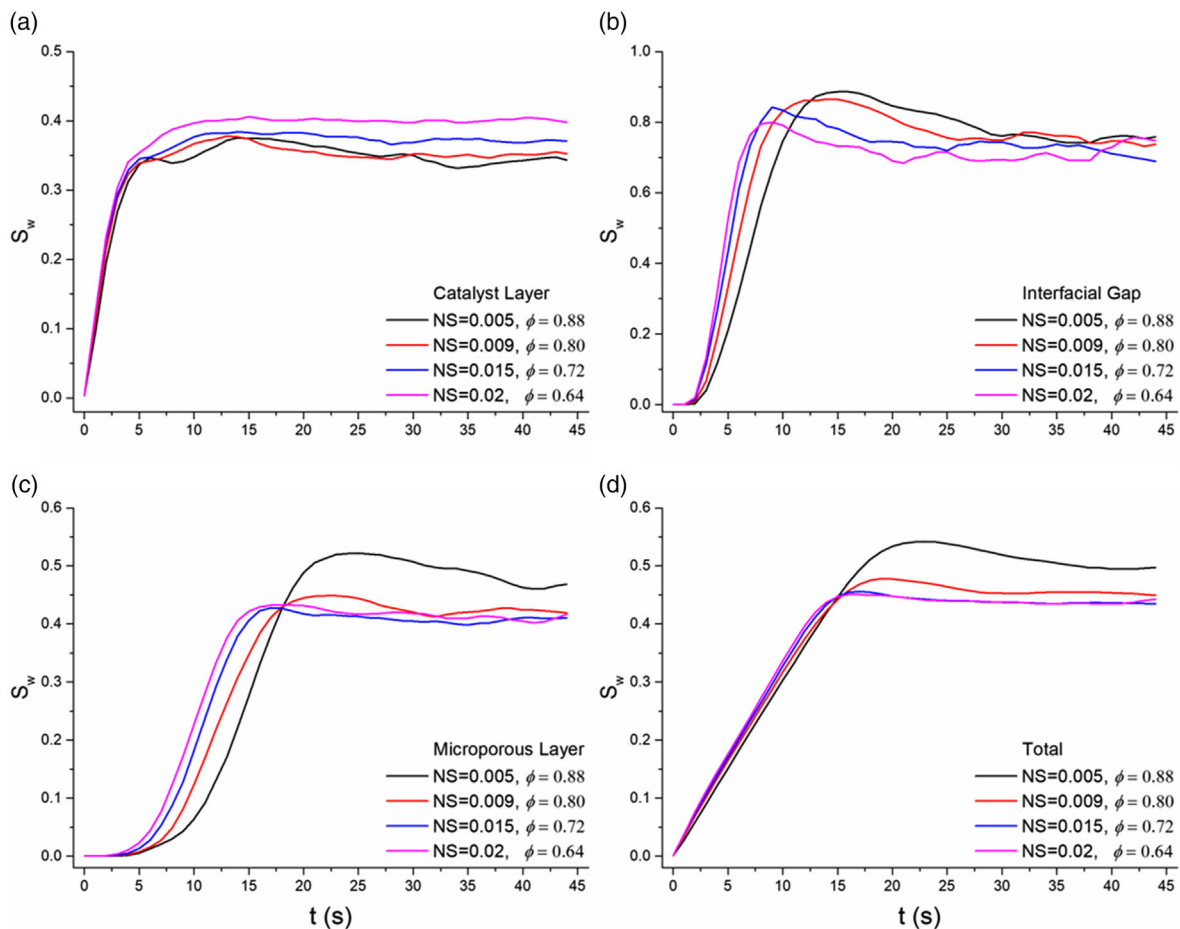


Figure 7. Temporal evolution of liquid saturation (S_w) with simulation group $\theta = 140^\circ$ and $\varphi = f(NS)$ for a) catalyst layer; b) interfacial gap; c) microporous layer; and d) total simulation domain.

compared to both experimental observation^[58] and numerical approach,^[59] where increasing compression ratio was found to decrease the liquid accumulation of GDL under the gas channel.

Figure 8 summarizes the average liquid saturation after reaching the maximum for simulation groups $\theta = 140^\circ$, $\varphi = 0.72$, and $\theta = 140^\circ$, $\varphi = f(NS)$, and the influence of porosity change on the liquid saturation is presented. First, liquid saturation fluctuation is more obvious for cases incorporating the porosity change than cases with $\varphi = 0.72$, especially at low compression stress such as $NS = [0.005, 0.009]$. For the catalyst layer, there is no significant difference in the liquid saturation for cases with $\varphi = 0.72$ and $\varphi = f(NS)$. The interfacial gap area strongly affects the liquid saturation in CL as different compression stress is applied. Increasing compression stress reduces the pore size of the interfacial gap, leading to increased liquid accumulation in the CL due to higher capillary pressure encountered at the MPL/CL interface. For the interfacial gap and microporous layer, higher liquid accumulation is found for cases with $\varphi = [0.8, 0.88]$ compared to $\varphi = 0.72$ under $NS = [0.005, 0.009]$. The results suggest the liquid transport is mainly influenced by the porosity of the pore space when applying different compression stress, where higher porosity cases have more liquid accumulation in the MPL and interfacial gap due to larger pore space. In addition, the porosity

change when applying different compression loadings should be incorporated for investigating liquid transport behaviors at PEMFC component layers.

3.3. Effects of Wettability

Wettability is important for the liquid transport and distribution inside the porous components of PEMFC. The contact angle variation of diffusion media is often observed due to the temperature change and hydrophobic coating content aging during long-term fuel cell operation.^[60,61] Here, the effects of contact angle on the liquid distribution and accumulation at MPL/CL interfacial region are investigated. Figure 9 presents the average liquid saturation after reaching the maximum value for simulation groups $\theta = 140^\circ$, $\varphi = [0.72]$; $\theta = 100^\circ$, $\varphi = [0.72]$; $\theta = 140^\circ$, $\varphi = f(NS)$; and $\theta = 100^\circ$, $\varphi = f(NS)$. Note the liquid saturation for case with $\theta = 140^\circ$ in Figure 9 could be slightly different from the results in Figure 8. As only one set of simulations are conducted for case with $\theta = 100^\circ$, its counterpart (one of the three sets simulation with $\theta = 140^\circ$) is applied to investigate the effects of wettability of liquid saturation.

For the catalyst and microporous layer, decreasing contact angle increases the liquid saturation at all compression loading

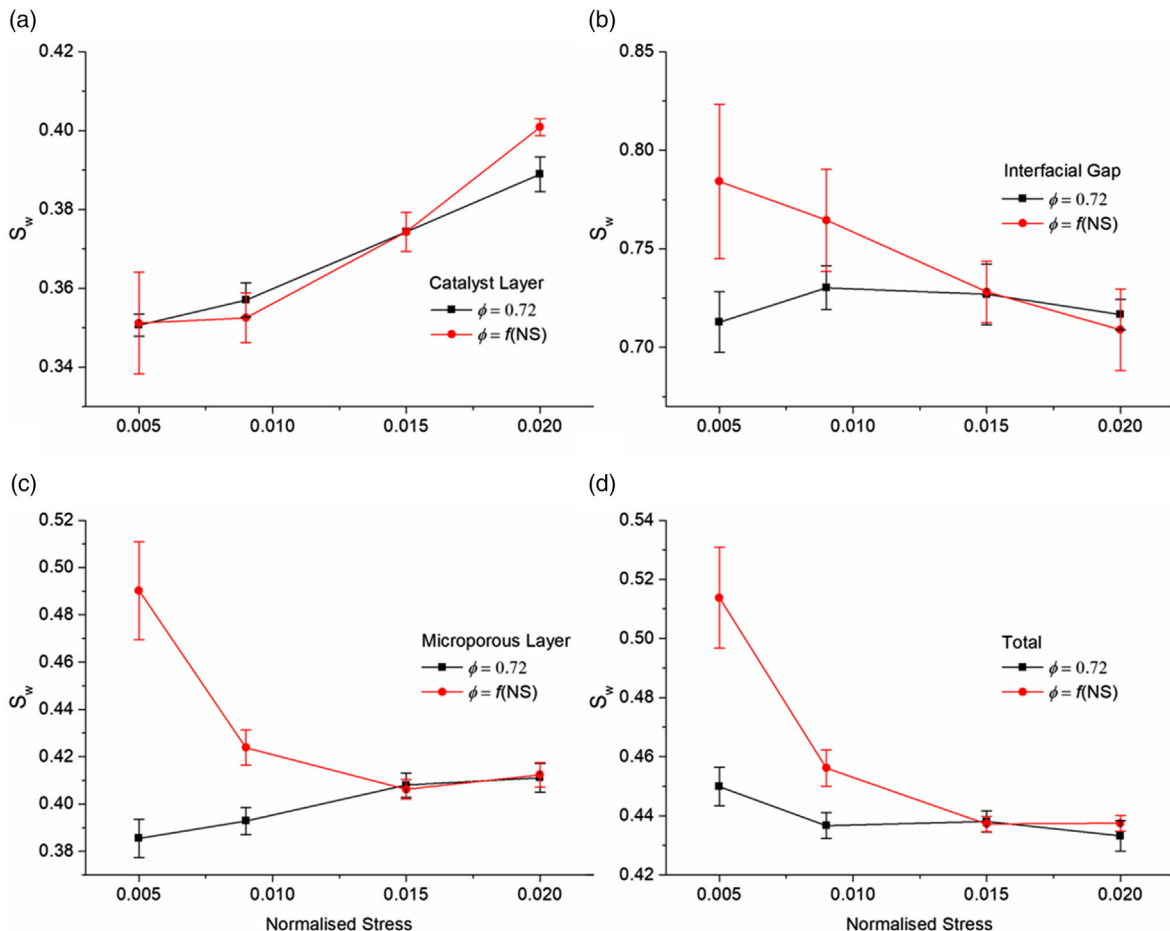


Figure 8. Average liquid saturation after reaching the maximum with simulation group $\theta = 140^\circ$, $\varphi = [0.72]$ and $\theta = 140^\circ$, $\varphi = f(NS)$ for a) catalyst layer; b) interfacial gap; c) microporous layer; and d) total simulation domain. The standard deviation for each case is calculated from three different simulations in Table 1.

conditions. By decreasing the contact angle from 140° to 100° , the water repellency of solid obstacles is decreased, resulting in the liquid accumulation increase in the CL and MPL. For the interfacial gap, the liquid saturation is significantly reduced by decreasing the contact angle. According to Equation (9), the capillary pressure is smaller for liquid flowing into MPL from the interfacial gap for the cases with $\theta = 100^\circ$ than cases with $\theta = 140^\circ$. Therefore, the interfacial gap is less saturated for cases with $\theta = 100^\circ$ as more liquid flow into the porous space of MPL. In terms of entire simulation domain, decreasing hydrophobicity increases the saturation for the simulation groups with $\varphi = [0.72]$, while the wettability effects on saturation are mixed for cases with $\varphi = f(NS)$. In addition, a reduction of saturation contrast between CL and gap region from around 0.4 to 0.2 is observed when the contact angle changes from 140° to 100° , indicating the heterogeneity of the liquid water distribution can be lowered by decreasing the material hydrophobicity.

The temporal evolution of liquid saturation for cases with $\theta = 140^\circ$ and $\theta = 100^\circ$ is presented in Figure 10 to illustrate further the influence of hydrophobicity on the liquid distribution at the interfacial region. The liquid saturation reaches maximum

value at $t = 10$ and 9 s for case with $\theta = 140^\circ$ and $\theta = 100^\circ$, respectively. The maximum liquid saturation for $\theta = 100^\circ$ is slightly lower than the case with $\theta = 140^\circ$, as plenty of water has entered the pore space of MPL shown in Figure 10b due to relatively lower breakthrough pressure required. The accumulated water in the interfacial gap quickly filled the pore space of MPL after the initial breakthrough, resulting a decline of liquid saturation for case $\theta = 100^\circ$, while a significant amount of liquid is still observed in the interfacial gap for case with $\theta = 140^\circ$ at $t = 13$ s. Afterward, the liquid saturation at interfacial gap for case $\theta = 100^\circ$ remains around 60% due to the fast liquid discharge from interfacial gap to MPL, and liquid saturation fluctuates between 70% and 80% for case with $\theta = 140^\circ$. Snapshots of liquid distribution at $t = 25$ s for both cases are presented in Figure 10b, where the liquid accumulation at the interfacial gap is less severe for the case with $\theta = 100^\circ$.

3.4. Relative Permeability of Liquid and Gas

The relative permeability of liquid water and gas throughout the liquid drainage process under various compression stress is examined to evaluate the liquid discharge and fuel supply

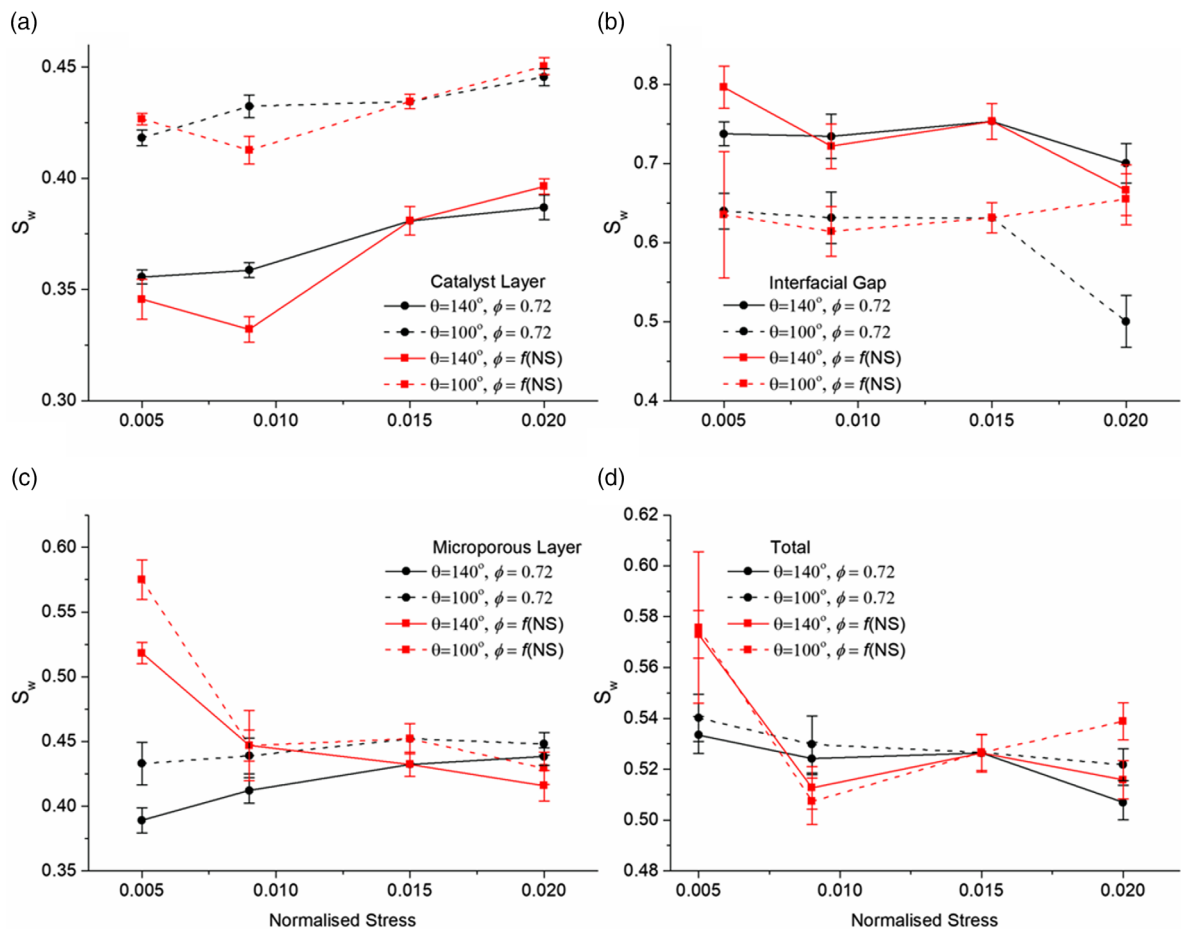


Figure 9. Average liquid saturation with simulation groups $\theta = 140^\circ, \phi = [0.72]; \theta = 100^\circ, \phi = [0.72]; \theta = 140^\circ, \phi = f(NS)$; and $\theta = 100^\circ, \phi = f(NS)$ for a) catalyst layer; b) interfacial gap; c) microporous layer; and d) total simulation domain.

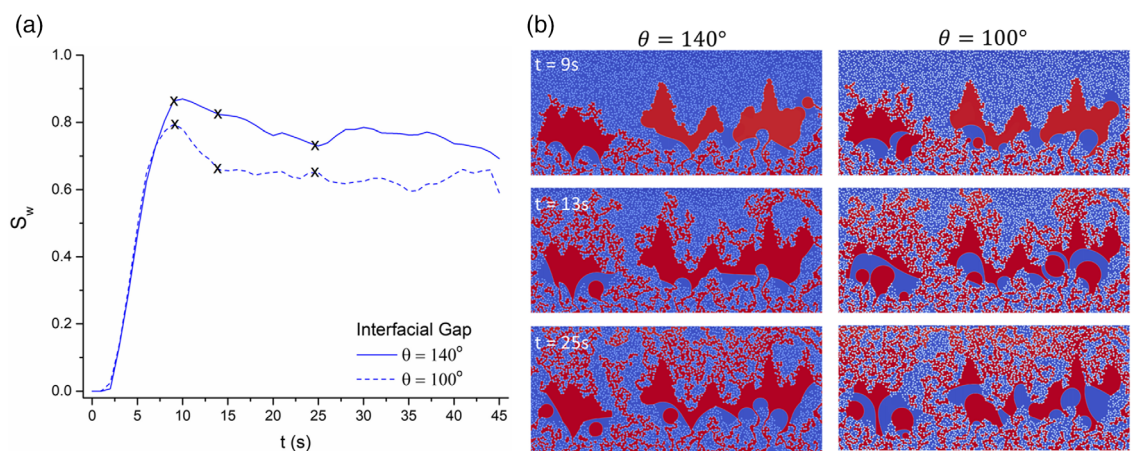


Figure 10. a) Temporal evolution of liquid saturation in the interfacial region for cases with $NS = [0.015], \varphi = [0.72]$. Solid line stands for $\theta = 140^\circ$ and dashed line for $\theta = 100^\circ$. Selected sections of liquid saturation profile at marked time steps are presented; b) snapshots of liquid distribution at $t = 9, 13$, and 25 s for both wetting conditions.

efficiency at the MPL/CL interfacial region. The relative permeability is correlated with the saturation level using the relative permeability equation^[62–64]

$$K_{rw/g} = S_{ew/g}^{\alpha} = \left(\frac{S_w/g - S_r}{S_{w,max} - S_r} \right)^{\alpha_{w/g}} \quad (10)$$

where $K_{rw/g}$ is the relative permeability of water/gas, S_e is the effective permeability, S_r is residual liquid saturation, and $S_{w,max}$ is the maximum liquid saturation. $\alpha_{w/g}$ is the fitting parameter for relative permeability evaluation, where smaller value means higher relative permeability for each phase. Theoretically, $\alpha_{w/g}$ is associated with the pore size distribution, where smaller value corresponds to a wider pore size distribution^[62]. Here, S_r is set to 0 as there is no residual water throughout the liquid invading process. **Figure 11** shows the relative permeability during the liquid drainage process for cases with fixed and varied porosities, and the intrinsic permeability of each interfacial region is also provided. Figure 11a,b presents the water and gas relative permeability for cases with $\theta = 140^\circ$, $\varphi = [0.72]$. The results suggest that the relative permeability of

both water and gas is strongly dependent on the saturation level. K_{rw} increases steadily from 0 to 0.5 with the increase of liquid saturation, and K_{rw} fluctuates at around $S_w = 0.3$ as liquid invading the interfacial gap area. K_{rg} decreases rapidly after the liquid starts to invade the pore space of CL, and K_{rg} finally reduced to 0.1 when the liquid saturation reaches the maximum. The fluctuation of K_{rg} is also observed at $S_w = 0.3$. The results suggest that for cases with $\varphi = [0.72]$, the compression stress has negligible influence on the liquid and gas permeability during the liquid displacement process, as there is no significant difference on the liquid saturation in the corresponding MPL/CL interfacial region. The MPL/CL interfacial gap could account for the relative permeability fluctuation in this work. As S_w is reaching 0.3, liquid mainly fills the pore space of interfacial gap, and the gas flux is regulated by flowing through the smaller pores in the porous material.

Figure 11c,d shows the liquid and gas relative permeability for cases incorporating the porosity change, and the results show a similar trend to the cases with $\varphi = [0.72]$. A slight difference is observed for the relative permeability of liquid, where the case of $NS = [0.005]$ with the highest saturation has the highest liquid

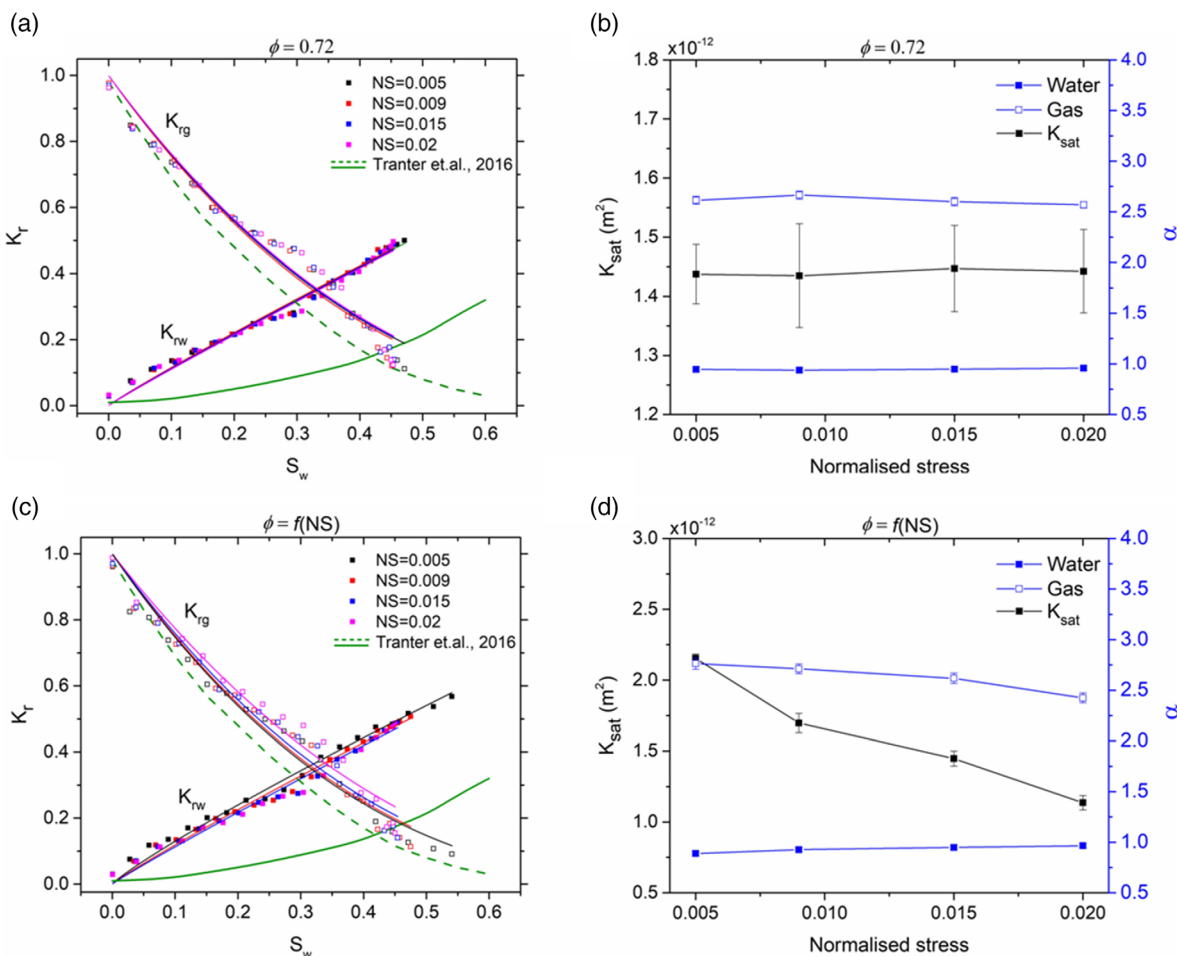


Figure 11. Relative permeability of liquid and gas phase throughout the liquid drainage process, with intrinsic permeability (K_{sat}) and fitting parameter α presented for cases with a,b) $\theta = 140^\circ$, $\varphi = [0.72]$ and c,d) $\theta = 140^\circ$, $\varphi = f(NS)$. Solid line stands for fitting curve of Equation (10) on the relative permeability. Green lines refer to the liquid and gas relative permeability with compression ratio = 0.3 and $\varphi = [0.71]$ in ref., [65] where compression ratio is defined as the percentage reduction in GDL layer thickness.

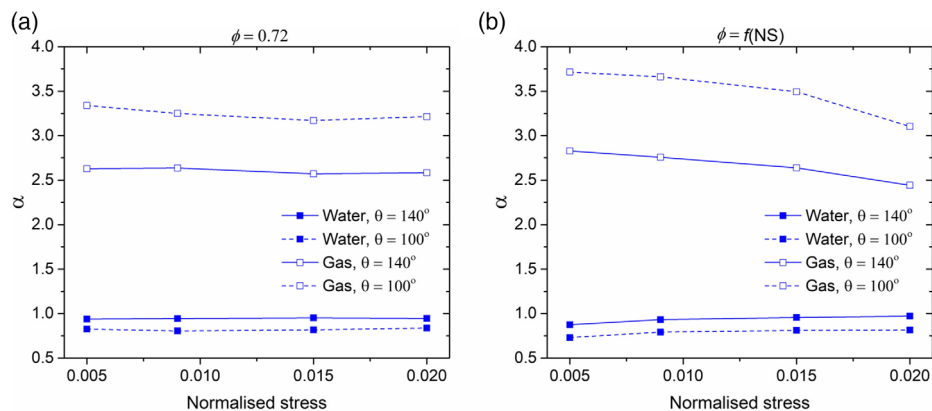


Figure 12. Liquid/gas permeability and fitting parameter α with contact angle $\theta = 140^\circ$ and $\theta = 100^\circ$ for cases a) $\phi = [0.72]$ and b) $\phi = f(NS)$.

relative permeability. For the gas phase, the relative permeability K_{rg} increases with the increase of compression loading, and the case of $NS = [0.02]$ has the highest gas relative permeability due to the potentially increased pathways for gas flow with the lowest liquid saturation level in the corresponding porous space. Therefore, increasing the compression loading facilitates the permeability of gas phase, while the water permeability through the interfacial region is less sensitive to the compression stress applied. The relative permeability of liquid and phase has been compared to the results from ref. [65] in which the gas relative permeability through the GDL layer under various compression ratios was investigated with a 3D model. It turned out the gas relative permeability in this work shows good agreement with the reported values in ref., [65] as shown in Figure 11. However, deviation in the liquid relative permeability between our results and reported values in ref. [65] is observed. The liquid relative permeability deviation could result from the difference in the pore size and porosity of the simulated porous media. It should also note that the simulations in this work are conducted in 2D, which can potentially lead to a slightly different representation of liquid and gas relative permeability compared with 3D observations due to varied percolation conditions.

The effects of wettability on liquid and gas relative permeability are further assessed in Figure 12a,b. Decreasing the contact angle increases the liquid permeability in the porous domain for all cases with $\phi = [0.72]$ and $\phi = f(NS)$ due to the increased liquid saturation, while gas permeability is suppressed with the decrease of wettability. The results suggest that the water relative permeability is highly dependent on saturation profile, and a strong hydrophobicity is preferred for the gas transport through the porous MPL/CL interface. The relative permeability results provide a qualitative analysis for effects of compression stress, material porosity, and wettability on the transport of liquid and gas phase, where high compression stress and hydrophobicity are found to facilitate the gaseous fuel supply process.

4. Conclusion

This article presents a numerical study on liquid and gas transport at the MPL/CL interfacial region, considering the

effects of compression stress, material porosity, and wettability. The numerical model is implemented with surface roughness, compression stress, and pore size distribution that match actual MPL/CL material properties. FEM (for interfacial contact mechanics) and LBM (for liquid transport and permeability calculation) are sequentially applied in the numerical framework. Different pore-scale displacement mechanisms resulted from capillary pressure difference are observed through the liquid drainage process. From the numerical simulations conducted, it is found that liquid transport characteristics under various compression loading conditions are mainly influenced by the capillary pressure difference due to interfacial gap area and material porosity change. The results suggest no significant difference in the liquid saturation or gas permeability is observed when only considering geometrical variations in the interfacial voids (cases with $\phi = 0.72$). For cases incorporating porosity change with various loading conditions, high compression stress facilitates liquid drainage and gas transport at the MPL/CL interface region, suggesting the necessity in incorporating the coupled hydromechanical analyses in fuel cell modeling. Moreover, strong hydrophobicity is desired for reducing the heterogeneity of the liquid water distribution at the interfacial region. The results highlight the contributions from the changes in interstitial voids, as well as from the porous MPL and CL layers, due to the mechanical compression, and are qualitatively comparable to observations from the existing literature.^[65] This study provides insights into applying appropriate compression level and wetting conditions at the MPL/CL interfacial region to optimize the water management and fuel supply during the PEMFC operation.

In this work, we mainly focus on the compression stress effects on fluid transport behaviors, where the assumptions and simplifications made here could be considered in future studies. First, 3D simulations adopting the practical pore-scale and surface features, e.g., from micro-XCT reconstructed geometries,^[66,67] should be considered for a more comprehensive representation of liquid and gas transport in PEM fuel cell layers. However, the computational cost of 3D representative cases may impede the capability of exploring the range of other physical parameters. Second, as PEMFCs usually operate at temperatures from 60 to 100 °C, nonisothermal flow conditions where water travels in both liquid and vapor phases need to be considered.

The potential phase transition of water, e.g., from liquid to vapor, or vapor to liquid, deserves to be implemented in the multiphase flow model to establish a more comprehensive understanding of fluid transport phenomena at PEMFC porous layers. Third, the MPL and CL material are assumed to have same wettability in this work. Nevertheless, the hydrophobicity of the porous diffusion media could be undermined due to the losses of the carbon materials or PTFE coating during the operation of PEMFCs, and leading to wettability heterogeneity of the diffusion materials.^[68] Therefore, the scenario that MPL and CL material have different hydrophobicity should be incorporated in the future investigation, with an emphasis on the effect of pore pressure variation at different diffusion layers on fluid transport behaviors in PEMFCs. Finally, the temporal and spatial variations of MPL and CL material properties due to shrinking, swelling, and rehydration^[69] could be further improved for capturing the pore-scale liquid displacement behaviors, in particular during cyclic operational conditions.^[70–72]

Supporting Information

Supporting Information is available from the Wiley Online Library or from the author.

Acknowledgements

This work was financially supported by Australian Government Research Training Program Scholarship. This research was undertaken with the assistance of the HPC service at the University of Sydney.

Open access publishing facilitated by The University of Sydney, as part of the Wiley - The University of Sydney agreement via the Council of Australian University Librarians.

Conflict of Interest

The authors declare no conflict of interest.

Data Availability Statement

The data that support the findings of this study are available from the corresponding author upon reasonable request.

Keywords

compression stress, lattice Boltzmann method, polymer electrolyte membrane fuel cells (PEMFCs), pore size distribution, surface roughness

Received: September 4, 2022

Published online: October 6, 2022

- [1] J. K. Lundquist, K. K. Duvivier, D. Kaffine, J. M. Tomaszewski, *Nat. Energy* **2019**, *4*, 26.
- [2] A. Siddiqi, L. D. Anadon, *Energy Policy* **2011**, *39*, 4529.
- [3] N. Kreifels, J. N. Mayer, B. Burger, C. Wittwer, *Energy Technol.* **2014**, *2*, 29.
- [4] J. M. Andújar, F. Segura, *Renewable Sustainable Energy Rev.* **2009**, *13*, 2309.
- [5] N. Bizon, *Int. J. Hydrogen Energy* **2014**, *39*, 10641.
- [6] J.-H. Wee, *Renewable Sustainable Energy Rev.* **2007**, *11*, 1720.
- [7] K. Jiao, X. Li, *Prog. Energy Combust. Sci.* **2011**, *37*, 221.
- [8] G. A. Futter, P. Gazdzicki, K. A. Friedrich, A. Latz, T. Jahnke, *J. Power Sources* **2018**, *391*, 148.
- [9] P. Yang, Y. Wang, Y. Yang, L. Yuan, Z. Jin, *Energy Technol.* **2021**, *9*, 2001012.
- [10] M. Afra, M. Nazari, M. H. Kayhani, M. Sharifpur, J. P. Meyer, *Energy* **2019**, *175*, 967.
- [11] H. K. Atiyeh, K. Karan, B. Peppley, A. Phoenix, E. Halliop, J. Pharoah, *J. Power Sources* **2007**, *170*, 111.
- [12] A. Mohseninia, D. Kartouzian, M. Eppler, P. Langner, H. Markötter, F. Wilhelm, J. Scholte, I. Manke, *Fuel Cells* **2020**, *20*, 469.
- [13] A. Mohseninia, D. Kartouzian, R. Schlumberger, H. Markötter, F. Wilhelm, J. Scholte, I. Manke, *ChemSusChem* **2020**, *13*, 2931.
- [14] C. Simon, J. Endres, B. Nefzger-Loders, F. Wilhelm, H. A. Gasteiger, *J. Electrochem. Soc.* **2019**, *166*, F1022.
- [15] S. S. Alwashdeh, I. Manke, H. Markötter, J. Haußmann, T. Arlt, A. Hilger, A. M. Al-Falahat, M. Klages, J. Scholte, J. Banhart, *Energy Technol.* **2017**, *5*, 1612.
- [16] T. Swamy, E. C. Kumbur, M. M. Mench, *J. Electrochem. Soc.* **2010**, *157*, B77.
- [17] I. V. Zenyuk, R. Taspinar, A. R. Kalidindi, E. C. Kumbur, S. Litster, *J. Electrochem. Soc.* **2014**, *161*, F3091.
- [18] F. E. Hizir, S. O. Ural, E. C. Kumbur, M. M. Mench, *J. Power Sources* **2010**, *195*, 3463.
- [19] S. Prass, S. Hasanpour, P. K. Sow, A. B. Phillion, W. Mérida, *J. Power Sources* **2016**, *319*, 82.
- [20] A. R. Kalidindi, R. Taspinar, S. Litster, E. C. Kumbur, *Int. J. Hydrogen Energy*, **2013**, *38*, 9297.
- [21] A. Turhan, S. Kim, M. Hatzell, M. M. Mench, *Electrochim. Acta* **2010**, *55*, 2734.
- [22] A. Z. Weber, M. A. Hickner, *Electrochim. Acta* **2008**, *53*, 7668.
- [23] C. Hartnig, I. Manke, R. Kuhn, N. Kardjilov, J. Banhart, W. Lehnert, *Appl. Phys. Lett.* **2008**, *92*, 134106.
- [24] S.-J. Lee, C.-D. Hsu, C.-H. Huang, *J. Power Sources* **2005**, *145*, 353.
- [25] R. W. Atkinson, Y. Garsany, B. D. Gould, K. E. Swider-Lyons, I. V. Zenyuk, *ACS Appl. Energy Mater.* **2018**, *1*, 191.
- [26] J. Ge, A. Higier, H. Liu, *J. Power Sources* **2006**, *159*, 922.
- [27] Z. Y. Su, C. T. Liu, H. P. Chang, C. H. Li, K. J. Huang, P. C. Sui, *J. Power Sources* **2008**, *183*, 182.
- [28] E. M. Khetabi, K. Bouziane, N. Zamel, X. François, Y. Meyer, D. Candusso, *J. Power Sources* **2019**, *424*, 8.
- [29] A. Bazylak, D. Sinton, Z.-S. Liu, N. Djilali, *J. Power Sources* **2007**, *163*, 784.
- [30] M. Fazeli, J. Hinebaugh, Z. Fishman, C. Tötzke, W. Lehnert, I. Manke, A. Bazylak, *J. Power Sources* **2016**, *335*, 162.
- [31] X. Zhou, Z. Niu, Z. Bao, J. Wang, Z. Liu, Y. Yin, Q. Du, K. Jiao, *J. Power Sources* **2019**, *437*, 226933.
- [32] H. Bajpai, M. Khandelwal, E. C. Kumbur, M. M. Mench, *J. Power Sources* **2010**, *195*, 4196.
- [33] Y. Bao, Y. Gan, *Int. J. Hydrogen Energy* **2020**, *45*, 17869.
- [34] A. Malekian, S. Salari, M. Tam, K. Oldknow, N. Djilali, M. Bahrami, *Int. J. Hydrogen Energy* **2019**, *44*, 18450.
- [35] M. S. Ismail, A. Hassanpour, D. B. Ingham, L. Ma, M. Pourkashanian, *Fuel Cells* **2012**, *12*, 391.
- [36] A. Akbar, J. Liu, S.-J. Chung, S. Um, *Renewable Energy* **2021**, *178*, 1106.
- [37] A. Akbar, S. Um, *Renewable Energy* **2022**, *194*, 195.
- [38] J. Becker, C. Wieser, S. Fell, K. Steiner, *Int. J. Heat Mass Transfer* **2011**, *54*, 1360.
- [39] X. Zhang, Y. Gao, H. Ostadi, K. Jiang, R. Chen, *Int. J. Hydrogen Energy* **2014**, *39*, 17222.
- [40] H. Yu, L. Bonville, R. Maric, *J. Electrochem. Soc.* **2018**, *165*, J3318.
- [41] K. K. Poornesh, C. Cho, *Int. J. Hydrogen Energy* **2011**, *36*, 3623.

- [42] M. Sabharwal, L. M. Pant, A. Putz, D. Susac, J. Jankovic, M. Secanell, *Fuel Cells* **2016**, *16*, 734.
- [43] W. Yoshimune, S. Kato, S. Yamaguchi, Y. Akimoto, A. Koizumi, H. Nakamura, *ACS Sustainable Chem. Eng.* **2021**, *9*, 7922.
- [44] C. Simon, D. Kartouzian, D. Müller, F. Wilhelm, H. A. Gasteiger, *J. Electrochem. Soc.* **2017**, *164*, F1697.
- [45] A. Rabbani, S. Jamshidi, S. Salehi, *J. Pet. Sci. Eng.* **2014**, *123*, 164.
- [46] X. Shan, H. Chen, *Phys. Rev. E* **1993**, *47*, 1815.
- [47] P. L. Bhatnagar, E. P. Gross, M. Krook, *Phys. Rev.* **1954**, *94*, 511.
- [48] R. Benzi, L. Biferale, M. Sbragaglia, S. Succi, F. Toschi, *Phys. Rev. E* **2006**, *74*, 021509.
- [49] Y. Gao, X. Zhang, P. Rama, R. Chen, H. Ostadi, K. Jiang, *Comput. Math. Appl.* **2013**, *65*, 891.
- [50] Z. Shi, Z. Wang, Y. Gan, *Adv. Water Resour.* **2021**, *149*, 103855.
- [51] L. Chen, Q. Kang, Y. Mu, Y.-L. He, W.-Q. Tao, *Int. J. Heat Mass Transfer* **2014**, *76*, 210.
- [52] P. P. Mukherjee, C.-Y. Wang, Q. Kang, *Electrochim. Acta* **2009**, *54*, 6861.
- [53] C. Zhou, L. Guo, L. Chen, X. Tian, T. He, Q. Yang, *Energies* **2021**, *14*, 3812.
- [54] M. J. Krause, A. Kummerländer, S. J. Avis, H. Kusumaatmaja, D. Dapelo, F. Klemens, M. Gaedtke, N. Hafem, A. Mink, R. Trunk, J. E. Marquardt, M.-L. Maier, M. Haussmann, S. Simonis, *Comput. Math. Appl.* **2021**, *81*, 258.
- [55] Z. Li, S. Galindo-Torres, G. Yan, A. Scheuermann, L. Li, *Adv. Water Resour.* **2018**, *116*, 153.
- [56] M. Nishita, S.-Y. Park, T. Nishio, K. Kamizaki, Z. Wang, K. Tamada, T. Takumi, R. Hashimoto, H. Otani, G. J. Pazour, V. W. Hsu, Y. Minami, *Sci. Rep.* **2017**, *7*, 1.
- [57] S. S. Datta, J. -B. Dupin, D. A. Weitz, *Phys. Fluids* **2014**, *26*, 062004.
- [58] K. Javaherdeh, M. Moslemi, H. R. Ashorynejad, *Heat Mass Transfer* **2022**, *1*.
- [59] Z. Bao, Y. Li, X. Zhou, F. Gao, Q. Du, K. Jiao, *Int. J. Heat Mass Transfer* **2021**, *178*, 121608.
- [60] M. Mortazavi, K. Tajiri, *J. Power Sources* **2014**, *245*, 236.
- [61] T. Arlt, M. Klages, M. Messerschmidt, J. Scholte, I. Manke, *Energy* **2017**, *118*, 502.
- [62] R. H. Brooks, *Hydraulic Properties of Porous Media*, Colorado State University, Fort Collins, Colorado **1965**.
- [63] Y. Mualem, *Water Resour. Res.* **1976**, *12*, 513.
- [64] M. Th. Van Genuchten, *Soil Sci. Soc. Am. J.* **1980**, *44*, 892.
- [65] F. Barbir, I. Tolj, G. Radica, *Fuel Cells* **2016**, *16*, 504.
- [66] A. Mularczyk, Q. Lin, D. Niblett, A. Vasile, M. J. Blunt, V. Niasar, F. Marone, T. J. Schmidt, F. N. Büchi, J. Eller, *ACS Appl. Mater. Interfaces* **2021**, *13*, 34003.
- [67] M. Maier, J. Dodwell, R. Ziesche, C. Tan, T. Heenan, J. Majasan, N. Kardjilov, H. Markötter, I. Manke, L. Castanheira, G. Hinds, P. R. Shearing, D. J. L. Brett, *J. Power Sources* **2020**, *455*, 227968.
- [68] S. Yu, X. Li, S. Liu, J. Hao, Z. Shao, B. Yi, *RSC Adv.* **2014**, *4*, 3852.
- [69] A. Sadeghi Alavijeh, S. Bhattacharya, O. Thomas, C. Chuy, Y. Yang, H. Zhang, E. Kjeang, *J. Power Sources* **2019**, *427*, 207.
- [70] N. Dyantyi, A. Parsons, P. Buollo, S. Pasupathi, *Mater. Renewable and Sustainable Energy* **2019**, *8*, 4.
- [71] R. L. Borup, J. R. Davey, F. H. Garzon, D. L. Wood, M. A. Inbody, *J. Power Sources* **2006**, *163*, 76.
- [72] A. Kannan, A. Kabza, J. Scholte, *J. Power Sources* **2015**, *277*, 312.